Inversion of airborne geophysics over the DO-27/DO-18 kimberlites — Part 1: Potential fields

Sarah G. R. Devriese[1], Kristofer Davis[1], and Douglas W. Oldenburg[1]

Abstract

The Tli Kwi Cho (TKC) kimberlite complex contains two pipes, called DO-27 and DO-18, which were discovered during the Canadian diamond exploration rush in the 1990s. The complex has been used as a testbed for ground and airborne geophysics, and an abundance of data currently exist over the area. We have evaluated the historical and geologic background of the complex, the physical properties of interest for kimberlite exploration, and the geophysical surveys. We have carried out 3D inversion and joint interpretation of the potential field data. The magnetic data indicate high susceptibility at DO-18, and the magnetic inversion maps the horizontal extent of the pipe. DO-27 is more complicated. The northern part is highly magnetic and is contaminated with remanent magnetization; other parts of DO-27 have a low susceptibility. Low densities, obtained from the gravity and gravity gradiometry data, map the horizontal extents of DO-27 and DO-18. We combine the 3D density contrast and susceptibility models into a single geologic model that identifies three distinct kimberlite rock units that agree with drilling data. In further research, our density and magnetic susceptibility models are combined with information from electromagnetic data to provide a multigeophysical interpretation of the TKC kimberlite complex.

Introduction

The Northwest Territories in Canada has been surveyed extensively for diamondiferous kimberlites since the early 1980s. The Lac de Gras region has been particularly productive, and it hosts two of the largest Canadian deposits: the Ekati and Diavik Diamond Mines. It is estimated that Canada has since become the world's third-largest diamond producer based on stone value (Natural Resources Canada, 2016), and more than 150 kimberlite pipes have been discovered in the region (Pell, 1997; McClenaghan et al., 2002).

Many different types of kimberlite exist within a pipe, and, unfortunately, there are several classifications and naming conventions (Pell, 1997; Kjarsgaard, 2007). Here, we divide kimberlitic rocks into three types based on their depositional environment:

1) hypabyssal (HK): intrusive, igneous, nonfragmented rock, root of volcanic pipe
2) volcaniclastic (VK): extrusive, fragmental, main volcanic body
3) pyroclastic (PK): a subclass of VK, extrusive, violent, deposited after an explosive event.

Figure 1a shows a simplified model of a kimberlite pipe after emplacement. In the Lac de Gras region, advancing glaciers removed much of the PK material and retreating glaciers deposited a glacial till layer. This is shown in the schematic specific to the Lac de Gras region (Figure 1b). The composition of the pipes exhibits different physical properties than those of the host rock and forms the basis for a geophysical exploration model.

At Lac de Gras, VK and PK generally have low density although some exceptions exist (Reed and Witherly, 2007), whereas HK has a slightly higher density. Overall, however, the density of a kimberlite is expected to be less than that of the background granitic rocks. HK and VK kimberlites tend to have higher magnetic susceptibilities than the host rock and PK kimberlite (Power and Hildes, 2007; Reed and Witherly, 2007). In addition, HK is often remanently magnetized (Clark, 1983; Macnae, 1985; Hargraves, 1989; Keating and Sailhac, 2004). High conductivities can result from weathering and serpentinization of VK and PK kimberlites (Power and Hildes, 2007). The physical property relationships, compared with the host rock, are summarized in Table 1. These contrasts in physical properties suggest that exploration can be conducted using geophysical surveys that acquire gravity, magnetic, and electromagnetic (EM) data.

With these expectations in mind, a reconnaissance airborne geophysical system was flown in 1992 that

[1]University of British Columbia, UBC-Geophysical Inversion Facility, Department of Earth, Ocean, and Atmospheric Sciences, Vancouver, Canada. E-mail: sdevries@eos.ubc.ca; kdavis@eos.ubc.ca; doug@eos.ubc.ca.

Manuscript received by the Editor 8 September 2016; revised manuscript received 5 January 2017; published online 18 April 2017. This paper appears in *Interpretation*, Vol. 5, No. 3 (August 2017); p. T299–T311, 17 FIGS., 4 TABLES.

http://dx.doi.org/10.1190/INT-2016-0142.1.

produced the sought-after geophysical fingerprints. The survey was located approximately 360 km northeast of Yellowknife, Northwest Territories, Canada, within the Archean Slave craton (Figure 2a). The frequency-domain EM system identified two coincident magnetic and EM anomalies, called DO-27 and DO-18, defining what was then and is still referred to as the Tli Kwi Cho (TKC) kimberlite complex.

In the years following the discovery, different geophysical surveys have been acquired and reacquired. Jansen and Doyle (2000) provide an overview of the many geophysical surveys that were collected over TKC prior to 2000. This leads to the kimberlite deposit serving as an important case study with two major parts. The first is the use of 3D geophysical inversion that incorporates minimal a priori information, to recover physical property models of density contrast, susceptibility, conductivity, and chargeability. The five geophysical surveys used in the inversions are summarized in Table 2; each survey has different parameters, such as line spacing and flight height. The second part concerns geologic interpretation from inversions with no a priori information. Each recovered 3D volume can be interpreted on its own, but the addition of subsequent recovered physical property models provides enhanced interpretation of the TKC geology. We specifically focus on unconstrained inversion with minimal a priori information (i.e., blind inversions) to assess the ability to interpret TKC using various geophysical data. In retrospect, these inversions would have provided valuable information to the geologic exploration program in the 1990s. Furthermore, we show that this is achievable through airborne geophysics alone, which can be more cost effective and faster to collect compared with ground surveys.

Our research is divided into three parts that focus on different physical properties and the challenges faced when interpreting the data. This paper, part 1, provides background about the deposit and examines potential field data. Data from airborne gravity gradiometry and three magnetic surveys as well as a ground gravity survey are inverted in three dimensions. Using the obtained physical property models, we produce and interpret a preliminary rock model for DO-27 and DO-18.

Part 2 (Fournier et al., 2017) focuses on recovering a conductivity model that is compatible with all three airborne data sets. The task is challenging due to strong induced polarization (IP) effects in the data, so a combination of 3D parametric and voxel-based inversions is used to obtain satisfactory results. The conductivity is combined with the density and the susceptibility to generate an updated rock model.

Part 3 (Kang et al., 2017) deals with IP effects in the EM data. The conductivity model is used to separate the EM and IP signals, and the extracted IP data are inverted to yield chargeability. This information, combined with the previous physical property models and their interpretation, further distinguishes the kimberlitic rocks in DO-18 and DO-27. The final interpretation, using all physical properties, is put into context with the current geologic data available.

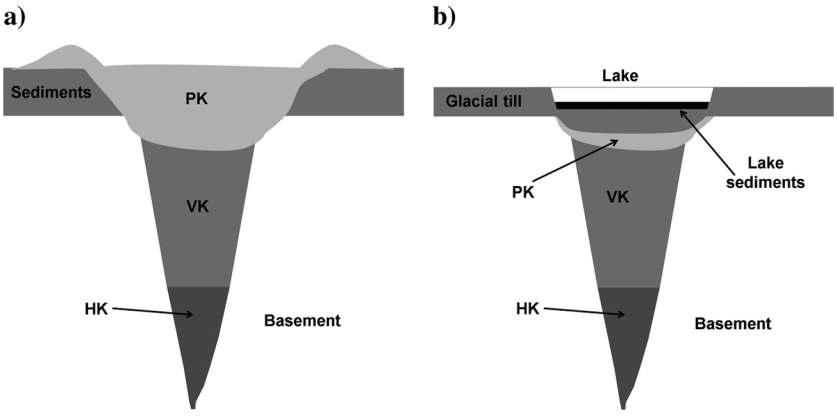

Figure 1. Schematic of a typical Lac de Gras kimberlite at (a) emplacement time and (b) after glaciation removed the top layers. A lake may be present after glaciation.

Table 1. Physical property relationships for the Lac de Gras region.

Rock type	Density	Susceptibility	Conductivity
Glacial till	Moderate	None	Moderate-high
Host rock	Moderate	None	Low
HK	Low-moderate	High	Low-moderate
VK	Low	Low-moderate	Moderate-high
PK	Low	Low-moderate	Moderate-high

Historical background and geologic setting

The early 1990s saw a rush to open Canada's first diamond mine, and in late 1992, a geophysical airborne survey discovered two kimberlites, called DO-18 and DO-27, as indicated by two magnetic and EM anomalies. Following the discovery, the interpretation of the TKC kimberlites evolved over five geologic models that are described in detail by Harder et al. (2009).

The surrounding lithology at TKC consists of post-Yellowknife Supergroup granite. A thin layer of mudstone covers the granites at the surface (Harder et al., 2008). The Wisconsinan glaciation (Dyke and Prest, 1987) covered the Lac de Gras region in glacial till and ultimately removed the mudstone and part of the kimberlites. The erosion that followed the glaciation left approximately 10%–20% of the TKC kimberlite complex exposed at the surface (Doyle et al., 1999), with

the rest below a layer of till 5–50 m thick. A lake was present above DO-27 during the acquisition of the geophysical data.

The latest model by Harder et al. (2009) hypothesized that DO-27 was created in multiple volcanic phases. HK kimberlite intrusions are found on the northeastern side of DO-27 from the initial phase, whereas a subsequent phase created VK kimberlite (Doyle et al., 1999). This VK was disturbed during another eruption, slightly to the southwest, which infilled most of the pipe with PK kimberlite. In contrast to its southern neighbor, DO-18 is a VK kimberlite; this supports the idea that its origin is distinctly different in geology and evolution from DO-27. Harder et al. (2008) and Doyle et al. (1999) conclude that DO-18 is not related to DO-27, despite their proximity.

The goal of our work is to determine how well our modern-day inversions of geophysical data compare with the latest geologic model. Although geologic and drilling information can be used to constrain the inversions, we specifically omit such a priori information from our inversions. Our goal is to investigate what geologic information can be provided by the geophysical data alone.

Geophysical inversion

To obtain quantitative information about 3D physical property distributions, geophysical data must be inverted. We provide a brief summary of our standard inversion methodology and refer the reader to the cited references for details.

The gravity and gravity gradiometry data are inverted using the methodologies outlined in Li and Oldenburg (1998) and Li (2001), respectively, whereas the inversion of magnetic data follows Li and Oldenburg (1996). The forward modeling for any of the potential fields is represented as a linear relationship between the discretized physical property model $\mathbf{m}$ and the observed data $\mathbf{d}$:

$$\mathbf{Gm} = \mathbf{d}, \tag{1}$$

where $\mathbf{G}$ is the sensitivity matrix ($\mathbf{m}$ was already defined before equation 1). The model is recovered by minimizing a global objective function ϕ:

$$\min \phi = \phi_d + \beta\phi_m, \tag{2}$$

where ϕ_d is the data misfit, ϕ_m is the model regularization, and the trade-off parameter β balances the two terms. The data misfit measures how well the recovered model reproduces the observed data:

$$\phi_d = \|\mathbf{W}_d(\mathbf{Gm} - \mathbf{d})\|_2^2, \tag{3}$$

where the diagonal matrix $\mathbf{W}_d$ contains the reciprocal of data uncertainties. The model objective function ϕ_m is defined as

$$\phi_m = \alpha_s\|\mathbf{W}_s(\mathbf{m} - \mathbf{m}_o)\|_2^2 + \sum_{i=1}^{3}\alpha_i\|\mathbf{W}_i(\mathbf{m} - \mathbf{m}_o)\|_2^2, \tag{4}$$

where $i = 1, 2, 3$ denotes the three spatial directions (x, y, z) and $\mathbf{m}_o$ is a reference model. The first term in ϕ_m controls how close the model is to the reference model, and the last three terms dictate smoothness in each spatial direction. The four α values regulate the relative importance of each term and balance units.

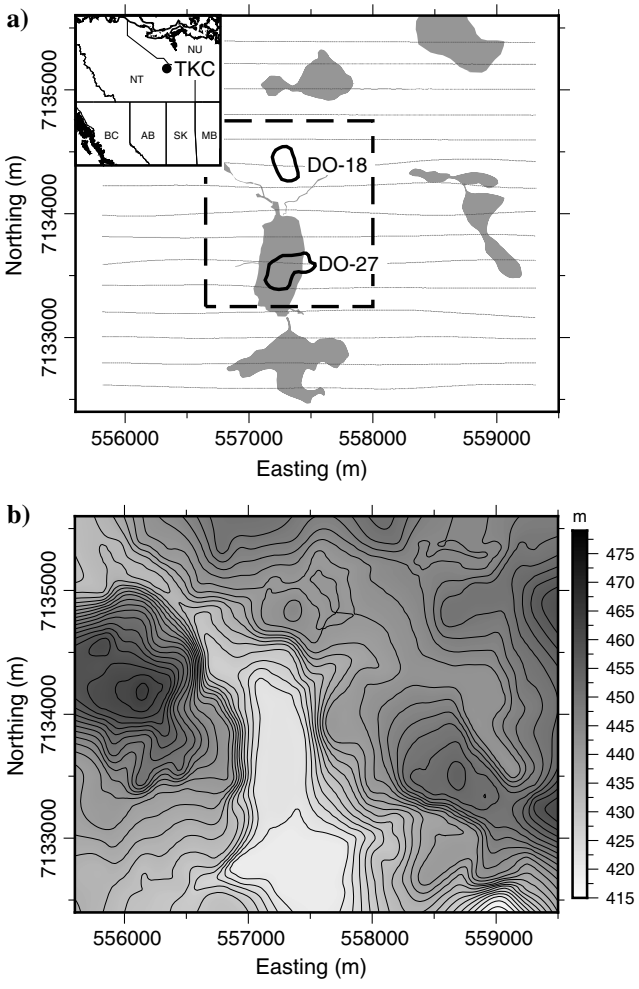

Figure 2. (a) Location of TKC kimberlite complex in Northwest Territories, Canada. The inset shows the map with reference to Canada. The dashed box outlines the region of interest. The gray lines indicate the DIGHEM flight lines, whereas the black outlines show the extent of DO-27 and DO-18 at the surface, based on drilling. (b) Topography model in the TKC survey region.

Table 2. Summary of the five different surveys used.

System	Year collected	Data collected
DIGHEM	1992	FEM, magnetics
Ground gravimeter	1994	Gravity
Falcon	2001	Gravity gradiometry
AeroTEM	2003	TEM, magnetics
VTEM	2004	TEM, magnetics

The **W** matrices can contain additional weighting or prior information. As well, $\mathbf{W}_i$ contains the discretized derivative with respect to each spatial direction. Details on how to form each matrix in the model objective function are given in the appendix of Li and Oldenburg (1996). A zero reference model was used throughout this work to imitate a true exploration scenario, in which prior information (e.g., drilling) is not available.

The global objective function is minimized to find a solution that minimizes structure and also provides an acceptable fit to the data. The trade-off parameter β can either be continuously cooled to yield a range of models from which the user can select a preferred solution, or a β can be sought that produces a model that generates a global desired misfit ϕ_d^*.

Table 3. Parameters for the airborne magnetic surveys.

System	DIGHEM	VTEM	AeroTEM
Flight line spacing (m)	200	75	75
Number of data	6274	26334	22561
Inclination (°)	83.0	83.3	83.0
Declination (°)	21.0	19.5	20.0
Field strength (nT)	59,500	59,580	59,500

Susceptibility

The first magnetic survey acquired at TKC used the DIGHEM system in 1992, which identified the two kimberlite pipes. Several follow-up surveys were flown (Jansen and Doyle, 2000) and included the AeroTEM and Versatile Time Domain Electromagnetic (VTEM) system. Table 3 provides the inclination, declination, field strength, and number of data for the three systems. All data were converted from their native coordinate systems to NAD27.

The DO-27 anomaly to the south and its northern smaller partner DO-18 are clearly visible in all three data sets (Figure 3a–3c), but the data contain regional trends. Any nonzero background may result in extra material (i.e., artifacts) in the recovered susceptibility model from inversion. Therefore, we subtracted a constant from the DIGHEM and VTEM magnetic data, such that the values away from the main anomalies were zero. The removal of a DC component was preferred over a polynomial fit because the latter can remove part of the kimberlite signal. In addition, only a subset of the DIGHEM and VTEM data sets that covered the area of interest was used. The resulting leveled data subsets are shown in Figure 3d and 3f, respectively.

With the AeroTEM magnetic data, each individual line had a varying DC shift. By comparing data points that have similar locations to those of the VTEM magnetic data, we leveled each line separately to obtain the processed AeroTEM magnetic data (Figure 3e).

Before inverting the processed data, we require an estimate of the data uncertainties (equation 3). Initial inversions indicated that an uncertainty of 1 nT for the DIGHEM and VTEM magnetic data allowed for the anomalies to be reproduced without generating the high-frequency structure that is characteristic of fitting noise in the data. The AeroTEM data are visibly noisier than the other two data sets, so a higher uncertainty of 2 nT was used. Our mesh for inversion consisted of a core region with 20 m cubic cells that was padded with cells increas-

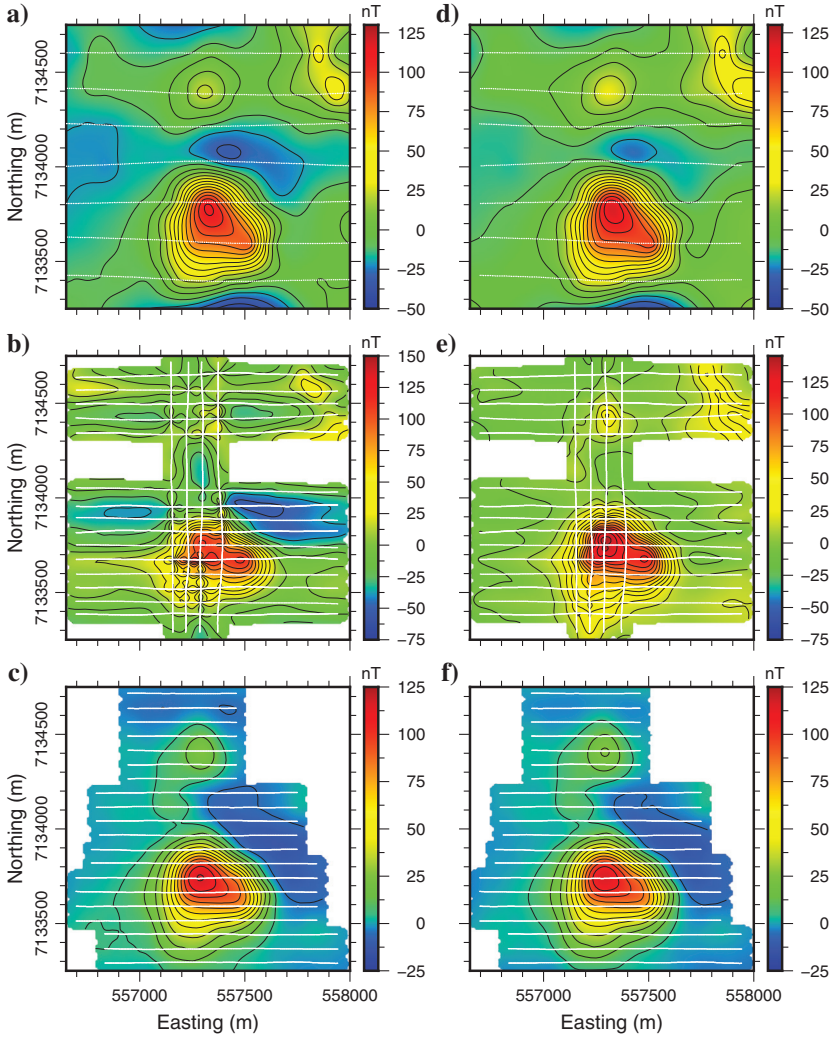

Figure 3. The subsets of the observed magnetic data from the (a) DIGHEM, (b) AeroTEM, and (c) VTEM surveys over the TKC kimberlites. The respective leveled magnetic data that were inverted are shown in (d-f).

ing in lateral size away from the core region. We set the α parameters to be $\alpha_s = 0.0001$, $\alpha_x = \alpha_y = \alpha_z = 1$; this made the four portions of the model objective function approximately the same. The Canadian Digital Elevation Data was used to model the topography (Figure 2b).

The recovered models from the inversion of each magnetic data set all globally fit the data ($\phi_d \approx 1$) and showed similar features, but they had different levels of resolution. For this reason and for brevity, we will only show the inversion result of the VTEM magnetic data because these data were the cleanest and were acquired at the highest resolution of the three surveys.

The recovered model is shown in Figure 4 as a plan-view slice at approximately 100 m below topography and as two cross sections: one through DO-18 (top right) and one through DO-27 (bottom right). The recovered susceptibility shows two distinct anomalies associated with the two kimberlite pipes, and it is very similar to the recovered model presented by Jansen and Doyle (2000). The northern DO-18 pipe has less volume and lower susceptibility than its neighbor to the south. DO-27 has a greater susceptibility and a shallow dip rather than the expected vertical pipe (Figure 1). Of note is that although the recovered model globally reproduces the observed data, there is a correlated misfit on the negative lobe to the northeast of DO-27 (Figure 5a). As such, induced magnetization may not completely explain the DO-27 anomaly, and we therefore examine the potential of remanent magnetization occurring within the kimberlite pipes.

Remanent magnetization

It is well-known that kimberlites can have remanent magnetization (Clark, 1983; Macnae, 1985; Hargraves, 1989; Keating and Sailhac, 2004). Unlike some kimberlites that are reversely magnetized and create large negative anomalies at high latitudes, in this case, it is not obvious that remanent magnetization is present. We tackle this question with two approaches. The first approach directly solves for a magnetization vector in three dimensions (Lelievre and Oldenburg, 2009). The second method approximates a bulk magnetization direction that will be used as a projection in the forward modeling and allows data to be inverted

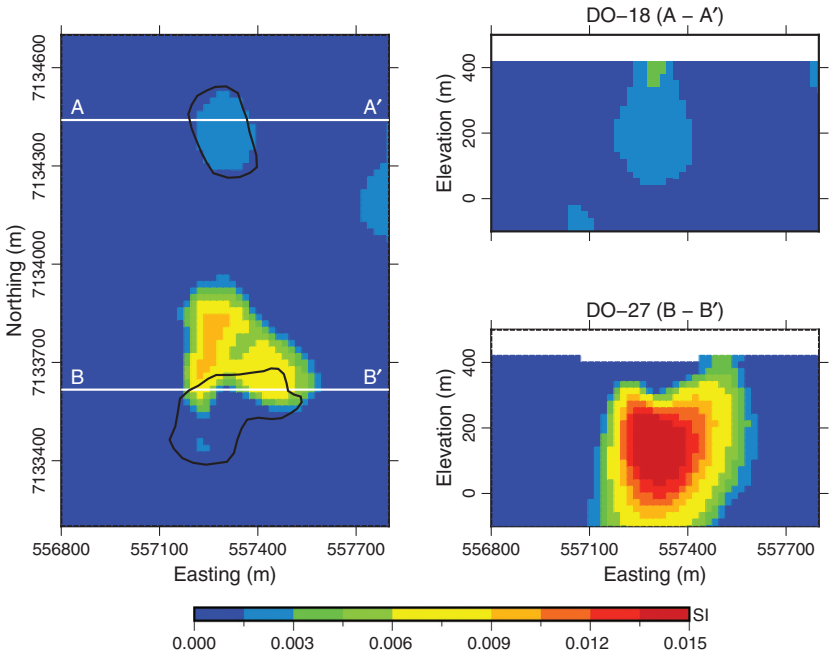

Figure 4. The recovered susceptibility model from the inversion of VTEM magnetic data assuming a purely induced magnetization. A plan-view depth slice of the model at an elevation of 330 m (approximately 100 m below topography) is shown on the left. The black outlines show the extent of DO-27 and DO-18 at the surface, based on drilling. The top right and bottom right panels show cross sections through DO-18 and DO-27, respectively.

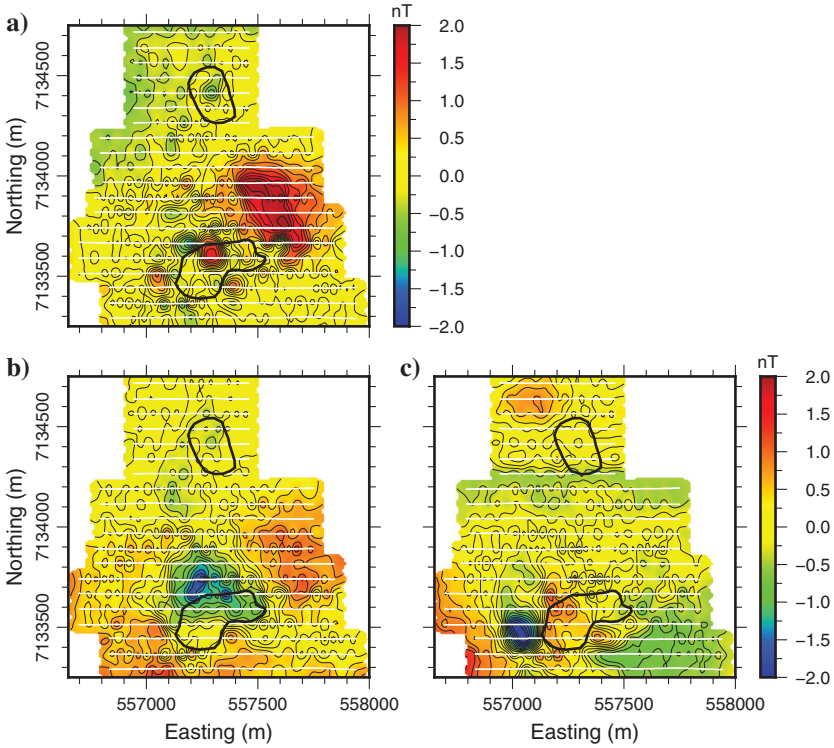

Figure 5. Data misfit between the observed and predicted VTEM magnetic data for the (a) induced inversion, (b) MVI, and (c) bulk-magnetization inversion. The correlated misfit observed in (a) shows the induced inversion cannot fit the data, whereas the inversions incorporating remanence in (b and c) produce much better results. The black outlines show the extent of DO-27 and DO-18 at the surface, based on drilling.

with the same methodology used in the previous section. We note that there are other methods available in the literature to estimate magnetization direction, and we refer the reader to Clark (2014) for a summary.

Magnetization vector inversion

We use the work of Lelievre and Oldenburg (2009) to invert for the magnetization vector in each principal direction. The magnetic vector inversion (MVI) follows the same general formulation as previously discussed in the methodology section. The difference is that the model contains the magnetization vector: $\mathbf{m} = [\mathbf{p}, \mathbf{s}, \mathbf{t}]^T$, where $\mathbf{p}$ is in the direction of the inducing field and $\mathbf{s}$ and $\mathbf{t}$ are the orthogonal components. Thus, the sensitivity is calculated for each component, so the total sensitivity $\mathbf{G} = [\mathbf{G}_p, \mathbf{G}_s, \mathbf{G}_t]$ and the forward modeling are described in equation 1. The directions $\hat{p}, \hat{s}$, and $\hat{t}$ make up the principal directions for the model objective function in equation 4.

The VTEM magnetic data are inverted using $\alpha_s = 0.0005, \alpha_x = 1, \alpha_y = 1, \alpha_z = 2$ to enforce equal weight on each component of the model objective function (equation 4). An extra weighting was placed on the $\mathbf{s}$ and $\mathbf{t}$ components to push them to their reference models of zero. That is, we try to recover a purely induced anomaly. The recovered effective susceptibility is shown in Figure 6. The northern anomaly (DO-18) reproduced a body indistinguishable from the result assuming only induced magnetization, indicating there is no need to assume that remanent magnetization plays a role here. Yet, for DO-27, the inversion recovered a remanent component to the northeast located near the negative lobe of the observed data.

To highlight differences between the MVI recovered model and the model obtained by assuming purely induced magnetization, we plot contours at $\kappa = 0.006$ SI in Figure 6. The dashed line pertains to the effective susceptibility from MVI, and the solid line is from the model in Figure 4. The contours show that the susceptibility anomaly at DO-27 has shifted northward when remanence is allowed. In addition, the data misfit (Figure 5b) shows that data in the northeastern part of DO-27, which were previously problematic, are now adequately fit. The anomaly, as a whole, however, is slightly underfit; this prompts us to also use an alternative method for including remanence in the inversion.

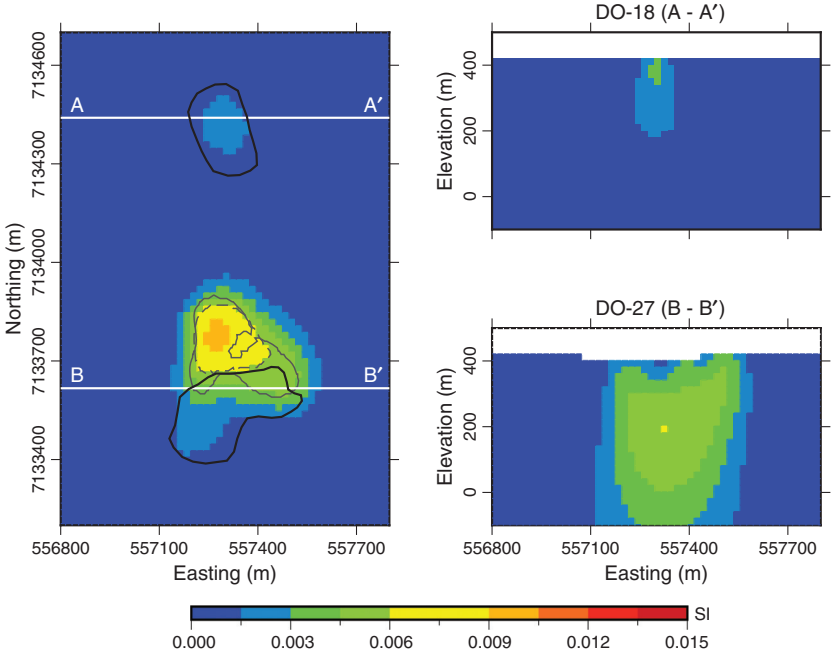

Figure 6. The recovered effective susceptibility model from the MVI of VTEM magnetic data. A plan-view depth slice of the model at an elevation of 330 m (approximately 100 m below topography) is shown on the left. The black outlines show the extent of DO-27 and DO-18 at the surface, based on drilling. The top right and bottom right panels show cross sections through DO-18 and DO-27, respectively. For reference, the contours of $\kappa = 0.006$ SI of the effective susceptibility (dashed gray) and the recovered model assuming an induced direction (solid gray) are given.

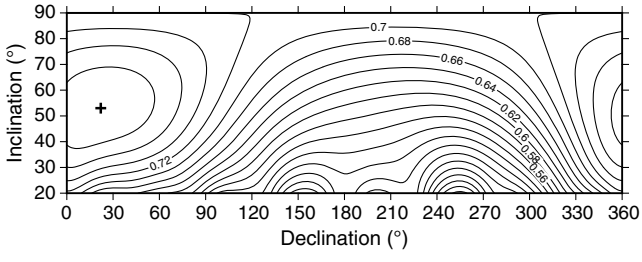

Figure 7. The results of the crosscorrelation of vertical and total gradients of RTP data with assumed inclinations and declinations. The maximum (marked with a black cross) is located at 53° inclination and 22° declination; the approximated remanent magnetization direction of DO-27.

Estimation of magnetization direction

In a second approach, we use the crosscorrelation method (Dannemiller and Li, 2006) to find a bulk magnetization direction. This is an extension, to three dimensions, of the work of Roest and Pilkington (1993). In this work, the data are reduced to the pole (RTP) via the Fourier transform with a range of assumed anomaly magnetization directions. Those magnetization directions that are not close to the true anomaly direction will create an incorrect, asymmetric, RTP field. The total gradient and vertical gradient of the RTP field will have more symmetry when the true anomaly magnetization direction is given, and thus the maximum crosscorrelation of the two will be achieved. We focus on DO-27 and calculate the crosscorrelation using VTEM magnetic data over a range of inclinations from 20° to 90° and all possible declinations in 1° increments. The results are

shown in Figure 7, and the black cross corresponds to the maximum value. The recovered inclination and declination were 53° and 22°, respectively. These values are within 10° of the recovered magnetization direction found within the anomaly core from MVI.

We reinvert the data, but use the estimated value for the direction of remanent magnetization when calculating the sensitivity matrix for forward modeling (equation 1). Thus, the sensitivities are generated assuming two directions of magnetization. In the region around DO-27, we use the remanent direction, and everywhere else the direction is assumed to be in the direction of the earth's field.

The data are inverted using the same α parameters as in the previous inversion. Images of the recovered model are given in Figure 8 along with a contour line at $\kappa = 0.006$ SI. The general shape of this model is similar to the effective susceptibility recovered from the MVI approach, although the overall susceptibility here is higher. Both inversions that include remanence pushed the anomaly at DO-27 to the north and have a less pronounced dip, compared with the inversion assuming only induced magnetization. This is an effect of being able to reproduce the negative data on the northeastern side of DO-27. The data misfit over the main anomaly is improved (Figure 5c) compared with the previous two inversions. There is some correlated misfit to the southwest, but the main anomaly and the region where large correlated misfits were initially observed are now quite well-fitted.

In summary, we have generated three magnetic susceptibility models that have distinct differences at DO-27, but they are the same over DO-18. All three inversions fit the data from a global misfit perspective, but a substantial correlated signal is observed in the misfit maps. The correlated misfit is reduced by assuming remanent magnetization over DO-27. Of the two inversions that include remanence, we choose the model obtained by fixing the direction of magnetization over DO-27 because the final misfit map only has a minor correlated feature.

Magnetic-susceptibility interpretation

We now generate a rock model based on our magnetic inversions and, in par-

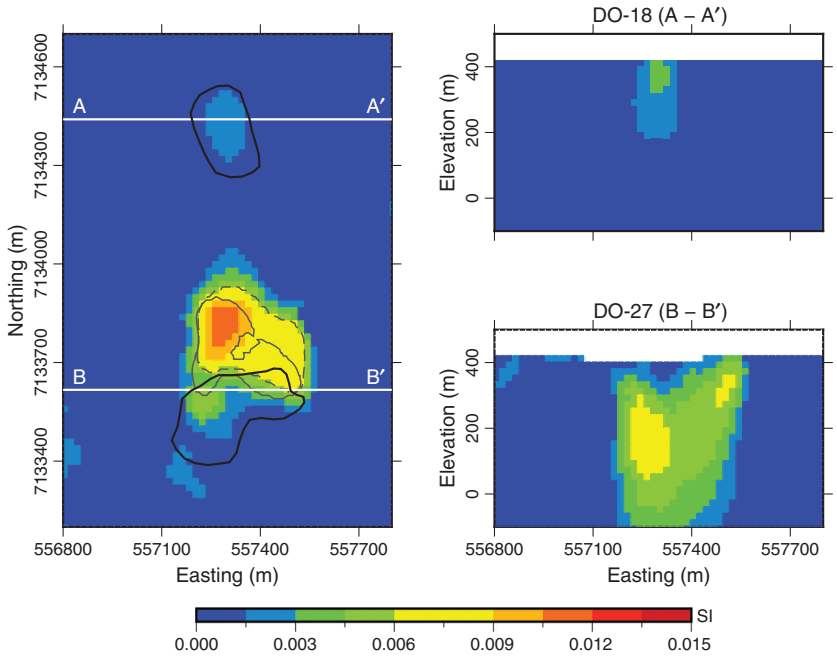

Figure 8. The recovered susceptibility model from the inversion of VTEM magnetic data assuming a remanent magnetization direction ($I = 53^{\circ}$ and $D = 22^{\circ}$). A plan-view depth slice of the model at an elevation of 330 m (approximately 100 m below topography) is shown on the left. The black outlines show the extent of DO-27 and DO-18 at the surface, based on drilling. The top right and bottom right panels show cross sections through DO-18 and DO-27, respectively. For reference, the contours of $\kappa = 0.006$ SI of the current model (dashed gray) and recovered model assuming an induced direction (solid gray) are given.

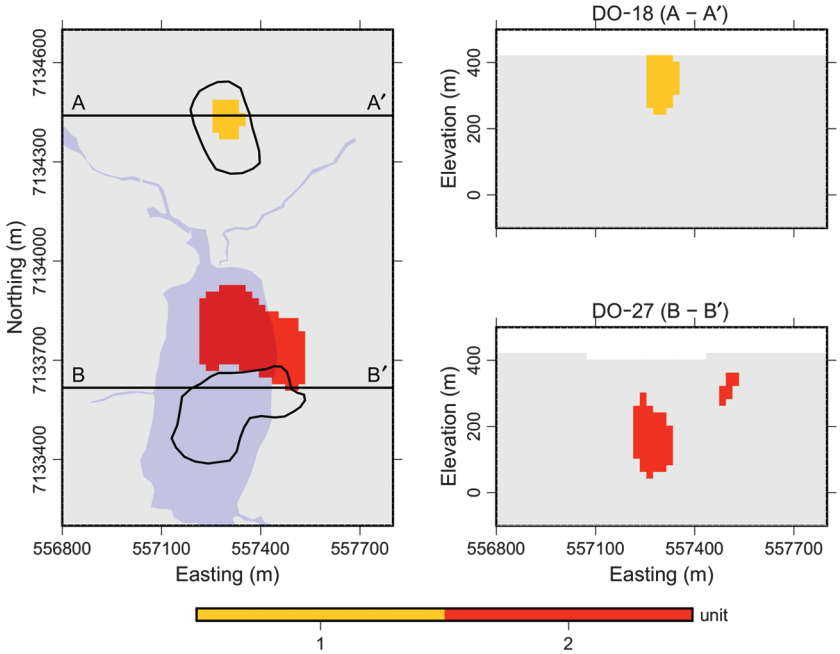

Figure 9. Interpretation of the recovered susceptibility model with two anomalous rock types: R1 at DO-18 and R2 at DO-27. A plan-view depth slice of the model at an elevation of 330 m (approximately 100 m below topography) is shown on the left. The black outlines show the extent of DO-27 and DO-18 at the surface, based on drilling. The top right and bottom right panels show cross sections through DO-18 and DO-27, respectively.

ticular, on the recovered susceptibility model in Figure 8. First, we note that DO-18 was recovered consistently in the inversions regardless of the assumption of remanent magnetization. This leads us to believe that it is likely not remanently magnetized, as seems to be the case for the recovered body at DO-27. Furthermore, the recovered susceptibility in DO-18 is smaller in magnitude than that for DO-27. These observations indicate that the two pipes contain different materials.

We note that DO-27 is asymmetric to the south and has a core of high susceptibility in the northern part of the anomaly. Given the geology, this could indicate two rock units within DO-27. However, the large susceptibility of the northern part can overshadow adjacent units of lesser susceptibility and make these units difficult to differentiate. That is, as the susceptibility changes from an anomalously high value to the background, it passes through all of the intermediate values. It can be difficult to determine whether those transition regions are representative units with a moderate value or if they are a consequence of the necessity to return smoothly to a background value, given the regularization used in the inversion.

This challenge is not addressed here, but rather we focus only on the high-susceptibility part of DO-27. Our resultant rock model in Figure 9 shows two anomalous units, R1 and R2. R1 is a vertical nondipping unit associated with all susceptibilities greater than 0.002 SI at DO-18, whereas R2 is associated with susceptibilities greater than 0.006 SI. It lies at the northern end of DO-27 and has a slight dip to the south.

If this interpretation were available in the early 1990s, it could have dispelled the notion that DO-18 and DO-27 have the same origin and are connected at depth. Furthermore, this information could have led to the third geology model that was developed in 1994. The second rock unit (R2) of our interpretation lies in the area that was originally drilled in the early 1990s. However, we now know that the original drilling missed the center of the DO-27 pipe. To get further insight about the extent of the pipe and why the original drilling should have been further south, we need additional information that can be provided by the density.

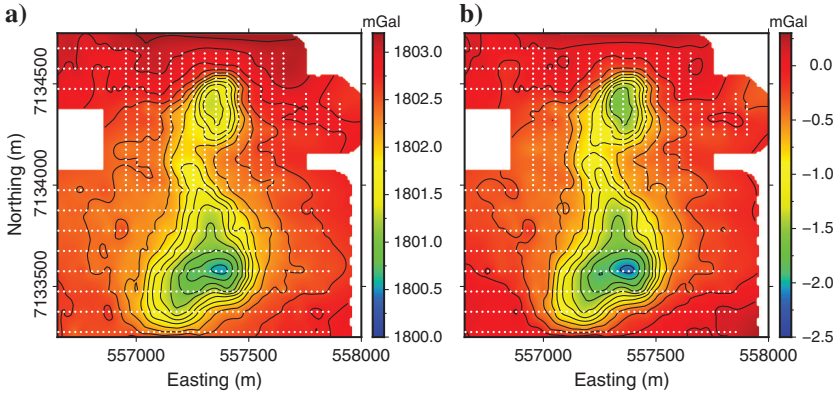

Figure 10. Observed (a) raw and (b) processed ground gravity data after removal of DC shift. Observation locations are denoted by the white dots.

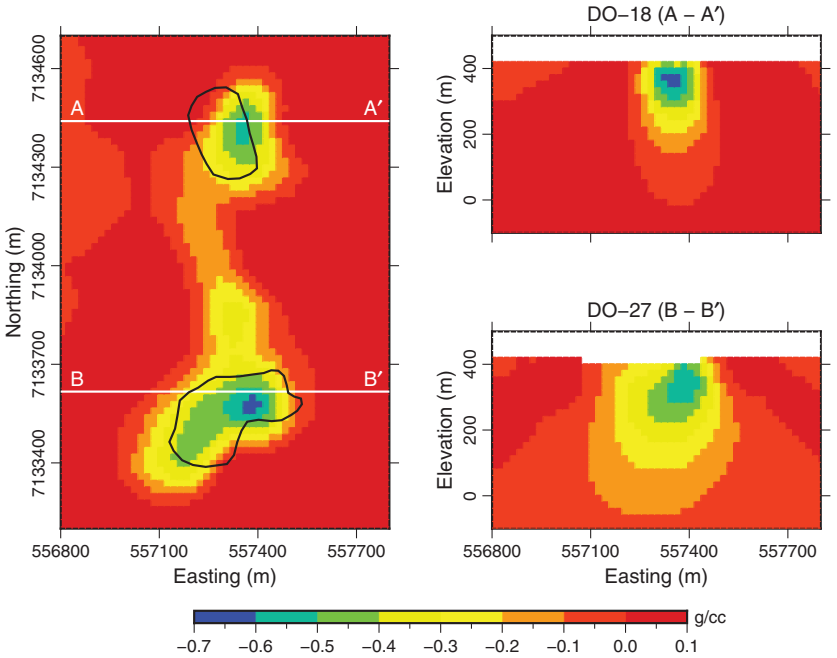

Figure 11. The recovered density contrast model from the inversion of the ground gravity data. A plan-view depth slice of the model at an elevation of 330 m (approximately 100 m below topography) is shown on the left. The black outlines show the extent of DO-27 and DO-18 at the surface, based on drilling. The top right and bottom right panels show cross sections through DO-18 and DO-27, respectively.

Density contrast

Ground gravity data were collected in 1994, two years after the initial discovery. A contour of these data is often used in the literature (e.g., Doyle et al., 1999; Harder et al., 2009). In addition, an airborne gravity gradiometry survey was acquired in 2001. For historical importance, we examine the ground gravity data first. Then, in keeping with the theme of airborne geophysics, we scrutinize the gravity gradiometry data.

Ground gravity

The ground gravity data were collected in the winter of 1994 in two different surveys. The surveys were leveled and combined into a single data set. Over DO-27, stations were spaced every 25 m in the easting direction and every 100 m

in the northing direction. Over DO-18, stations were collected every 50 m in the easting direction and every 25 m in the northing direction. This gives a total of 972 locations, and these were converted from their native coordinate system to NAD27 prior to processing. We note that elevation data were only provided for the southern survey. Thus, for simplicity, we use the same elevation model (Figure 2b) that was used for the magnetic inversions.

Three main features are observed in the gravity data (Figure 10a): low-gravity anomalies over DO-27 and DO-18 and a low-gravity anomaly connecting the two kimberlite pipes. The gravity data hover at approximately 1800 mGal, from which we subtracted a regional field of 1803 mGal, such that the data away from any anomalies are zero (Figure 10b). We determine, after running the initial inversions, that 0.045 mGal is an appropriate uncertainty level for these data, and we invert the data using the same mesh that was used to recover the susceptibility. The results, presented in Figure 11, have a substantial negative density contrast in the area of the two pipes and a smaller negative contrast between them.

Two major challenges were faced in using the ground gravity data. The first problem was the missing elevation over DO-18, and the assumptions that were required to calculate that information. The second drawback became evident when comparing the data with the gradiometry data. The center of the DO-18 anomaly differed by approximately 100 m (two ground survey lines) between the two data sets, suggesting that the two ground surveys may not have been stitched together accurately. Despite the potential errors in location, we view the ground gravity as a valid contribution (Jansen and Doyle, 2000), but we have more confidence in the accuracy of the gravity gradiometry data.

Gravity gradiometry

Airborne gravity gradiometry data were collected in 2001 using the Falcon system, with the final product being the vertical component (G_{zz}). The survey line spacing was approximately 50 m. A terrain correction density of 2.67 g/cm^3 and a 100 m wavelength cutoff filter were applied to the data. We converted the locations from their native coordinate system to NAD27 before plotting and inverting. The three features that were observed in the ground data are also present here (Figure 12a). In total, 2 eotvos were subtracted from the observed data before inverting (Figure 12b).

We assigned an uncertainty of 5 eotvos obtained by calculating the standard deviation of the westmost line of data, which was considered to be in the background and away from the kimberlites. The mesh contained 20 and 10 m cells in the horizontal and vertical directions, respectively, and the topography used is shown in Figure 2b. The recovered density contrast model (Figure 13) contains the two kimberlite pipes as well as a conduit with low-density material extending north-

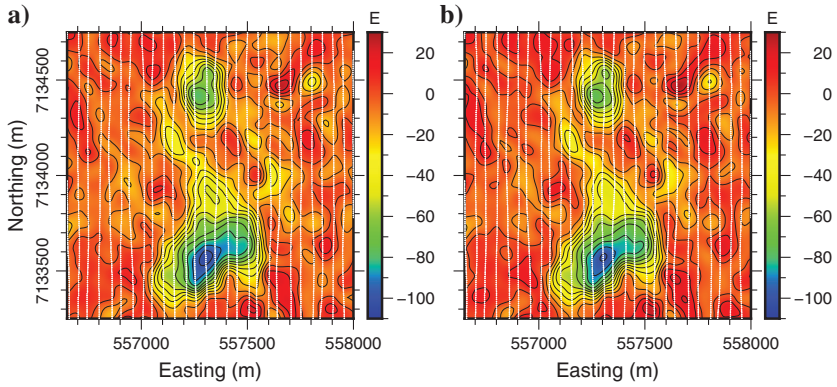

Figure 12. Observed (a) raw and (b) processed airborne gravity gradiometry data (G_{zz}) after removal of a 2 eotvos DC shift. Observation locations are denoted by the white dots.

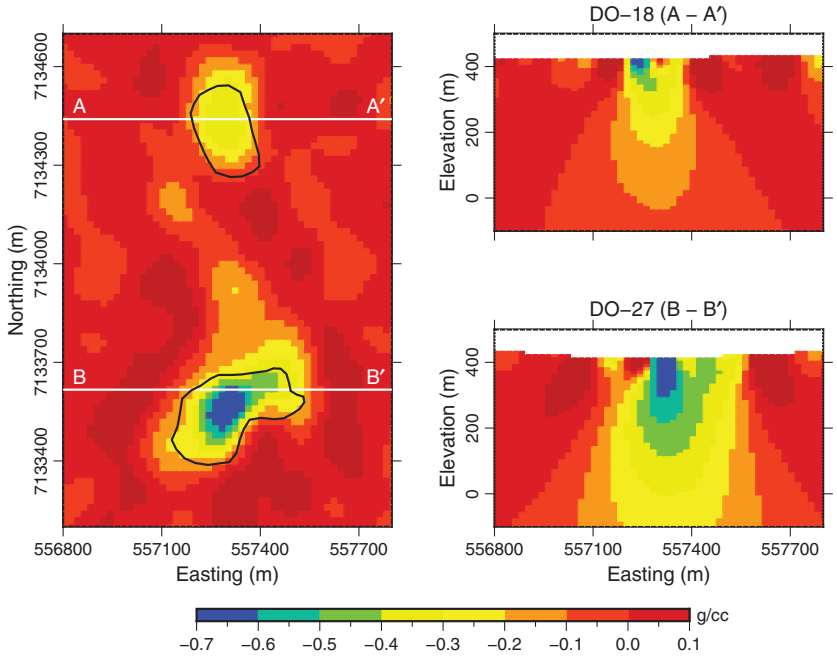

Figure 13. The recovered density contrast model from the inversion of the gravity gradiometry data. A plan-view depth slice of the model at an elevation of 330 m (approximately 100 m below topography) is shown on the left. The black outlines show the extent of DO-27 and DO-18 at the surface, based on drilling. The top right and bottom right panels show cross sections through DO-18 and DO-27, respectively.

ward from DO-27 (similar to that of the gravity result). The near-surface fluctuations in density contrast can also be observed in the data.

Density contrast interpretation

We focus the interpretation on the model recovered from inverting the airborne gravity gradiometry data. As is characteristic for this region, the kimberlite material is less dense than the surrounding host rock (Power and Hildes, 2007). The density contrast model shows two low-density volumes, kimberlites that are not connected at depth. In addition, the kimberlites appear to be vertical, as expected for a typical Lac de Gras kimberlite (Figure 1). The DO-27 has an "arm" extending toward the north, which could be either kimberlite or glacial till from the retreating glaciers as discussed by Harder et al. (2009).

Peregrine has drilled many holes at DO-27, evaluated the logged core, and generated a 3D density model (Eggleston et al., 2014). In Figure 14, we have replotted a cross section through the model but first subtracted a background density of 2.67 g/cm^3. Our recovered model agrees nicely with the density estimates. Due to smooth regularization defined in equation 4, the recovered kimberlite is wider and smoother than the density discontinuity at the pipe boundary in the density estimate.

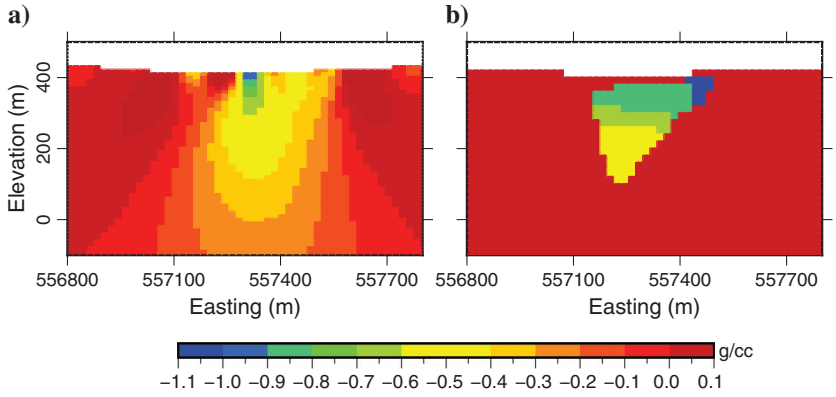

Figure 14. Comparison of (a) the cross section through DO-27 shown in Figure 13 and (b) the density estimate from Eggleston et al. (2014), which has been converted into density contrast assuming a density of 2.67 g/cm^3 for the background granitic rock.

Using a cut-off value of −0.24 g/cm^3, we generate an initial rock model for the TKC complex based on the gravity gradiometry inversion (Figure 15). This result shows that the DO-27 pipe further extends to the south than was originally modeled using the magnetic data alone. The density contrast, whether obtained from the surface gravity survey or the airborne gradiometry survey, could have immediately showed that the initial drilling was on the edge of the pipe instead of sampling its core and may have prevented the initial size misinterpretation of the southern pipe.

The density contrast model only provides information about the spatial extents of the kimberlite pipes; it does not reveal information about the different types of kimberlitic rocks within DO-18 and DO-27. To accomplish this, we need to jointly interpret the density and susceptibility models.

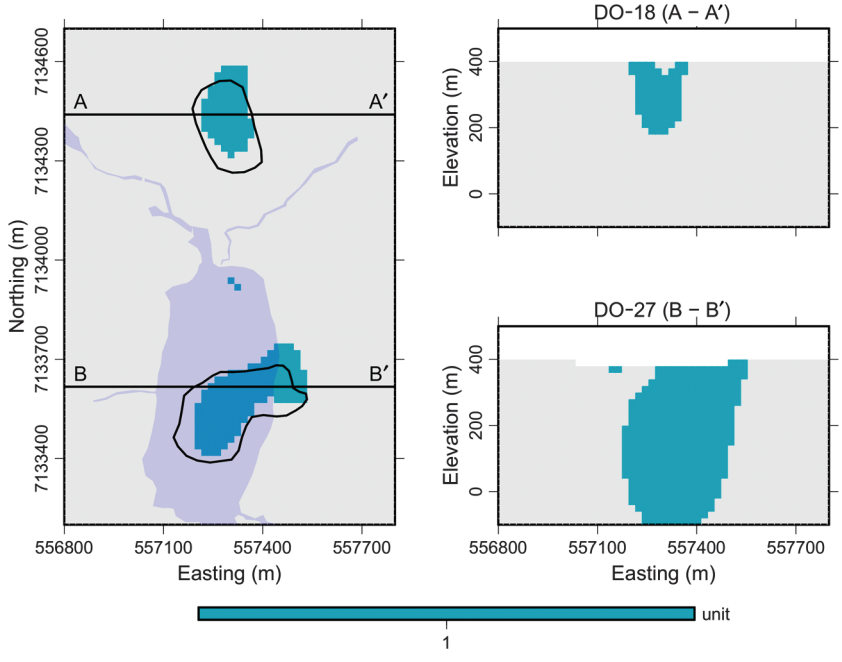

Figure 15. Interpretation of the recovered density contrast model showing two kimberlite pipes. A plan-view depth slice of the model at an elevation of 330 m (approximately 100 m below topography) is shown on the left. The black outlines show the extent of DO-27 and DO-18 at the surface, based on drilling. The top right and bottom right panels show cross sections through DO-18 and DO-27, respectively. The density shows DO-18 and DO-27, but it does not provide enough information to differentiate their composition.

Interpretation

The inversion results obtained thus far allow us to define a background and three rock units that are associated with kimberlites. These are delineated in Table 4. The background rock, identified as R0, has a reference density of 2.67 g/cm^3 and no susceptibility. Kimberlitic rocks have a low density and a low, medium, or high susceptibility. Different combinations of these density and susceptibility values yield rock types R1, R2, and R3. The R1 unit has no, or low, susceptibility (less than 0.002 SI); this is unlike R2 and R3. The R3 unit is less dense than the background, but it has a

greater density than R2. In addition, R3 contains a different magnetic orientation than the inducing field, whereas R2 is purely induced. The composition of these two kimberlitic rocks is further distinguished by their different susceptibilities: R2 ranges between 0.002 and 0.006 SI, whereas R3 has susceptibilities greater than 0.006 SI.

By applying these classifications to our inversion models, we obtain a rock model with three distinct anomalous rock units (Figure 16): DO-18 appears as a small body consisting of R2, whereas DO-27 is predominantly R1, with R3 on the northeastern edge of the pipe.

We wish to associate a geologic lithology with each rock unit. From the literature, the rocks of interest in the Lac de Gras region consist of PK, VK, HK, till, and background. The relative physical property values of these units were addressed at the beginning of this paper and are summarized in Table 1. Using these relationships, we identify R3 as HK kimberlite (high magnetic susceptibility and low to moderate density). R1 and R2 differ with respect to susceptibility, with R1 being lower. On this basis, we separated them into different units, but to identify their kimberlitic lithology, we need additional information. Using the geology information from Harder et al. (2008), we further classify R1 as a PK kimberlite and R2 as xenocryst-rich VK kimberlite (XVK), which is a subset of VK. The till layer was not identified using the potential field data.

The drilling programs that resulted in the density estimate (Eggleston et al., 2014) also identified four different kimberlitic rocks: HK, VK, and PK kimberlite at DO-27 and XVK at DO-18. We generated a model using the drilling data, shown in Figure 17, and compared it with our final interpretation (Figure 16). Our rock model from geophysical inversions clearly resembles the ground truth. Specifically, the recovered PK (R1) unit at DO-27 agrees well with the drilling. The drilling confirms the HK (R3) unit on the north end of DO-27, but the inversion of potential field data did not allow for discrimination of the VK (R4) unit. In addition, the magnetic and gravity inversions did not recover the till layer at the surface (unit R5), which is likely due to the lack of a physical property contrast from the background and/or a lack of depth resolution. At DO-18, the drilling confirms R2 as XVK. The comparison between the rock model and the drilling also shows that the inversion nicely recovered the size and extents of the two kimberlites and, particularly, the different kimberlitic rocks within DO-27. The interpretation of the different rock units at DO-27 and DO-18 is summarized in Table 4.

Table 4. The inversions of airborne magnetic and gravity gradiometry data identify the background granitic rock and the major kimberlitic rock units: PK and HK at DO-27 and XVK at DO-18. The VK at DO-27 is indistinguishable as is the till layer given the potential field methods. The colors identify the rock types in Figures 16 and 17.

	Rock unit	Density contrast (g/cm^3)	Susceptibility (SI)	Remanence	Rock type
	R0	> −0.24	0	×	Host
	R1	<= −0.24	< 0.002	×	PK
	R2	<= −0.24	0.002 – 0.006	×	XVK
	R3	> −0.24	> 0.006	✓	HK
	R4	-	-	-	VK
	R5	-	-	-	Till

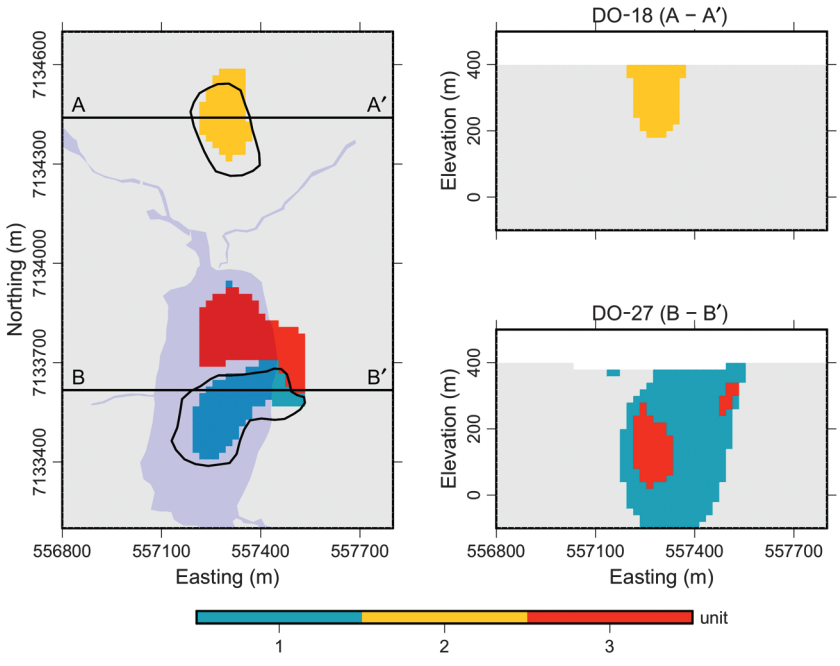

Figure 16. Joint interpretation from recovered models derived from gravity gradiometry and magnetic data. Each of the three distinct rock units is considered to be a type of kimberlite, with the main differences being the magnitude and the magnetic orientation of the susceptible material. A plan-view depth slice of the model at an elevation of 330 m (approximately 100 m below topography) is shown on the left. The black outlines show the extent of DO-27 and DO-18 at the surface, based on drilling. The top right and bottom right panels show cross sections through DO-18 and DO-27, respectively.

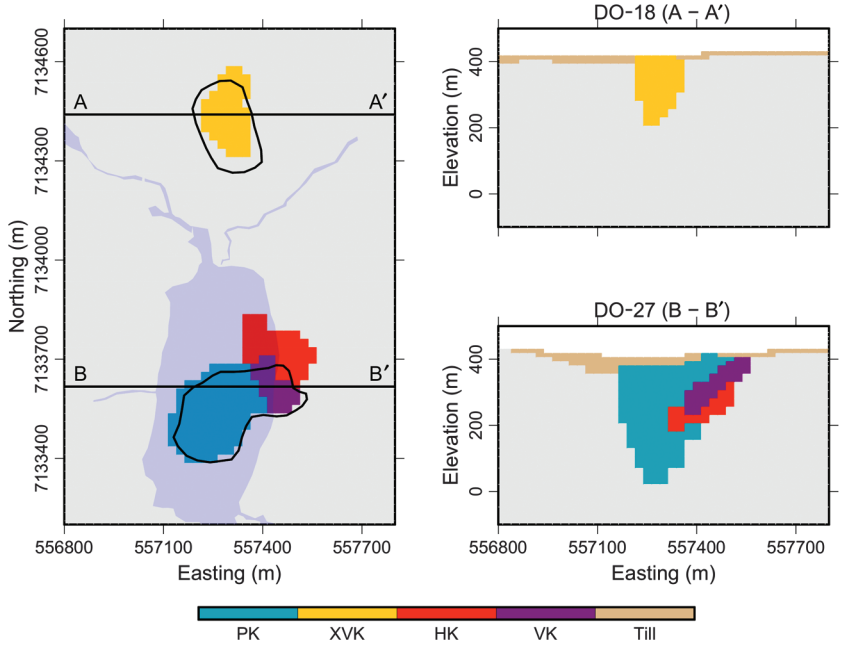

Figure 17. Drilling model showing a plan-view depth slice at an elevation of 330 m (approximately 100 m below topography) is shown on the left. The black outlines show the extent of DO-27 and DO-18 at the surface, based on drilling. The top right and bottom right panels show cross sections through DO-18 and DO-27, respectively. Table 4 describes each rock type in more detail.

Conclusion

We have presented the inversion of ground gravity, airborne gravity gradiometry, and airborne magnetic data over the TKC kimberlites. The recovered models describe the shape and depth extent of the two pipes and agree well with drilling. The southern kimberlite, DO-27, is a low-density rock unit with a highly susceptible portion in the north. In contrast, DO-18 primarily has low density, with moderate portions of susceptible material. Given the geophysical information, we were able to distinguish these two bodies from the background country rock. Our results are similar to those previously published, but we also explore the possibility of remanent magnetization within DO-27. This results in an improved fit to the data, and it changes the shape of the kimberlite.

We created a geologic model based upon the two physical properties and identified three distinct rock units. With input from geology, we were able to identify these as being PK and HK kimberlites at DO-27, and a XVK kimberlite at DO-18. A comparison of our rock model with known geology obtained from drilling shows that we have recovered valuable information about the geometry of the pipe and location of the PK and HK units. We reiterate that our results, with the exception of the geologic lithology assignment, were obtained by using only airborne data and by implementing blind inversions that did not incorporate a priori information specific to the deposit. Therefore, this work can be used as an example of what might be obtained in surveys at other locations that have not yet had ground exploration carried out. In a subsequent paper in this series, we further develop this goal by analyzing airborne EM data to extract information about conductivity and chargeability. Those physical property models, combined with the results in this paper, generate a rock model that is even more representative of the TKC complex.

Acknowledgments

The authors would like to thank K. Witherly and J. Jansen for the stimulating discussions about the TKC data sets over the last 15 years and for identifying the challenges for inverting and interpreting these data. We also thank J. Pell, B. Clements, B. Doyle, T. Arvanis, and R. Enkin for discussions about the data and geologic interpretations. We especially thank Condor Geophysics, Peregrine Diamonds, and Kennecott for making the data sets available for our research. We sincerely thank the three reviewers (J. Jansen, J. McNae, and one anonymous) for their comments and for helping to improve this work. Finally, we are indebted to other UBC-GIF members for their efforts on this two-year project: D. Fournier, S. Kang, M. S. McMillan, D. Bild-Enkin, N. Corcoran, D. Cowan, L. Heagy, D. Marchant, L. A. C. Mata, M. Mitchell, and D. Yang.

References

Clark, D. A., 1983, Comments on magnetic petrophysics: Bulletin of the ASEG, **14**, 49–62, doi: 10.1071/EG983049.

Clark, D. A., 2014, Methods for determining remanent and total magnetizations of magnetic sources — A review: Exploration Geophysics, **45**, 271–304, doi: 10.1071/EG14013.

Dannemiller, N., and Y. Li, 2006, A new method for determination of magnetization direction: Geophysics, **71**, no. 6, L69–L73, doi: 10.1190/1.2356116.

Doyle, B. J., K. Kivi, and B. H. S. Smith, 1999, The Tli Kwi Cho (DO27 and DO18) diamondiferous kimberlite complex, Northwest Territories: Proceedings of the 7th International Kimberlite Conference, 194–204.

Dyke, A. S., and V. K. Prest, 1987, Late Wisconsinan and Holocene history of the Lauren-tide ice sheet: Geographie Physique et Qauternaire, **41**, 237–263, doi: 10.7202/032681ar.

Eggleston, T., K. Brisebois, and J. Pell, 2014, Lac de Gras project Northwest Territories, Canada: NI 43-101 Technical Report, Peregrine Diamonds Ltd.

Fournier, D., D. S. Kang, M. S. McMillan, and D. W. Oldenburg, 2017, Inversion of airborne geophysics over the DO-27/DO-18 kimberlites — Part 2: Electromagnetics: Interpretation, **5**, this issue, doi: 10.1190/int-2016-0140.1.

Harder, M., C. M. Hetman, M. C. Baumgartner, and J. Pell, 2008, The preliminary geology of the DO-18 kimberlite, Lac de Gras kimberlite province, Canada: Presented at the 9th International Kimberlite Conference.

Harder, M., B. H. Scott Smith, C. M. Hetman, and J. Pell, 2009, The evolution of geological models for the DO-27 kimberlite, NWT, Canada: Implications for evaluation: Lithos, **112**, 61–72, doi: 10.1016/j.lithos.2009.06.024.

Hargraves, R. B., 1989, Paleomagnetism of mesozoic kimberlites in Southern Africa and the Cretaceous apparent polar wander curve for Africa: Journal of Geophysical Research, **94**, 1851–1866, doi: 10.1029/JB094iB02p01851.

Jansen, J. C., and B. J. Doyle, 2000, The Tli Kwi Cho Kimberlite Complex, Northwest Territories: A Geophysical Post Mortum.

Kang, D. S., D. Fournier, and D. W. Oldenburg, 2017, Inversion of airborne geophysics over the DO-27/DO-18 kimberlites — Part 3: Induced polarization: Interpretation, **5**, this issue, doi: 10.1190/int-2016-0141.1.

Keating, P., and P. Sailhac, 2004, Use of the analytic signal to identify magnetic anomalies due to kimberlite pipes: Geophysics, **69**, 180–190, doi: 10.1190/1.1649386.

Kjarsgaard, B. A., 2007, Kimberlite pipe models: Significance for exploration: Proceedings of exploration 2007: 5th Decennial International Conference on Mineral Exploration, 667–677.

Lelievre, P. G., and D. W. Oldenburg, 2009, A 3D total magnetization inversion applicable when significant, complicated remanence is present: Geophysics, **74**, no. 3, L21–L30, doi: 10.1190/1.3103249.

Li, Y., 2001, 3-D inversion of gravity gradiometer data: 71st Annual International Meeting, SEG, Expanded Abstracts, 1470–1473.

Li, Y., and D. W. Oldenburg, 1996, 3-D inversion of magnetic data: Geophysics, **61**, 394–408, doi: 10.1190/1.1443968.

Li, Y., and D. W. Oldenburg, 1998, 3-D inversion of gravity data: Geophysics, **63**, 109–119, doi: 10.1190/1.1444302.

Macnae, J., 1985, Applications of geophysics for the detection and exploration of kimberlites and lamproites: Journal of Geochemical Exploration, **53**, 213–243, doi: 10.1016/0375-6742(94)00057-I.

McClenaghan, M. B., B. C. Ward, I. M. Kjardsgaard, D. E. Kerr, and L. A. Dredge, 2002, Indicator mineral and till geochemical dispersal patterns associated with the Ranch lake kimberlite, Lac de Gras region, NWT, Canada: Geochemistry: Exploration, Environment, Analysis, **2**, 299–320.

Natural Resources Canada, 2016, Canada: A diamond-producing nation: http://www.nrcan.gc.ca/mining-materials/diamonds/15972, accessed 14 November 2016.

Pell, J. A., 1997, Kimberlites in the Slave Craton, northwest territories, Canada: Geoscience Canada, **24**, 77–91.

Power, M., and D. Hildes, 2007, Geophysical strategies for kimberlite exploration in northern Canada: Proceedings of Exploration 2007: 5th Decennial International Conference on Mineral Exploration, 1025–1031.

Reed, L. E., and K. E. Witherly, 2007, 50 years of kimberlite geophysics: A review: Proceedings of exploration 2007: 5th Decennial International Conference on Mineral Exploration, 679–689.

Roest, W., and M. Pilkington, 1993, Identifying remanent magnetization effects in magnetic data: Geophysics, **58**, 653–659, doi: 10.1190/1.1443449.

Biographies and photographs of the authors are not available.